

Supporting Information

Unveiling the phonon scattering mechanisms in half-Heusler thermoelectric compounds

Ran He^{a,*,#}, Taishan Zhu^{b,#}, Yumei Wang^c, Ulrike Wolff^a, Jean-Christophe Jaud^d, Andrei Sotnikov^a, Pavel Potapov^a, Daniel Wolf^a, Pingjun Ying^a, Max Wood^e, Zhenhui Liu^{a,f}, Le Feng^{a,f}, Nicolas Perez Rodriguez^a, G. Jeffrey Snyder^e, Jeffrey C. Grossman^b, Kornelius Nielsch^{a,f,g,*}, and Gabi Schierning^{a,*}

^aLeibniz Institute for Solid State and Materials Research, Dresden, 01069, Germany

^bDepartment of Materials Science and Engineering, Massachusetts Institute of Technology, Cambridge, MA 02139, USA

^cInstitute of Physics, Chinese Academy of Sciences, Beijing 100190, China

^dDepartment of Materials and Earth Sciences, Technical University of Darmstadt, Darmstadt, 64287, Germany

^eDepartment of Materials Science and Engineering, Northwestern University, Evanston, Illinois 60208, USA

^fInstitute of Applied Physics, Technical University of Dresden, Dresden, 01062, Germany

^gInstitute of Materials Science, Technical University of Dresden, Dresden, 01062, Germany

#Equal contributors

*To whom correspondence should be addressed:

r.he@ifw-dresden.de

g.schierning@ifw-dresden.de

k.nielsch@ifw-dresden.de

I. Experimental

Sample Preparation

This work investigates the thermoelectric performance of half-Heusler compounds with compositions $\text{ZrCoSb}_{1-x}\text{Sn}_x$, $\text{Zr}_{1-y}\text{Ti}_y\text{CoSb}$, and $\text{ZrCo}_{1-z}\text{Fe}_z\text{Sb}$ ($x=0, 0.02, 0.04, 0.06, 0.08, 0.1, 0.12, 0.14, 0.16, 0.2, 0.25$, and 0.3 ; $y=0, 0.1, 0.2$, and 0.3 ; $z=0, 0.06, 0.1, 0.15$). In general, 15 grams of raw elements, including Zr sponge (99.5%, MaTeck), Ti sponge (99.95%, Alfa Aesar), Co powder (99.9%, MaTeck), Fe powder (99.5%, Alfa Aesar), Sb broken rod (99.8%, Alfa Aesar) and Sn powder (99.5%, Alfa Aesar), are weighted according to the stoichiometry in an Ar-filled glovebox with O_2 and H_2O levels lower than 1 ppm. The weighed raw elements are ball milled for 30 hours by a SPEX 8000D machine using hardened steel vials and two $\phi 12$ mm tungsten carbide balls with powder loosening on the 10th and the 20th hour. Subsequently, the ball-milled powders are compacted using a field-assisted sintering technique (FAST, FCT Systeme GmbH) at 1323 K and 50 MPa for 3 minutes. The entire sintering is carried out under vacuum. The sintered compounds are cut and polished to the desired sizes for thermoelectric transport measurement.

Two special samples with composition $\text{ZrCoSb}_{0.8}\text{Sn}_{0.2}$ are synthesized for comparison purposes. One of the samples is sintered at 1473 K and 50 MPa for 30 minutes to enlarge the grain size. The other sample starts from weighing the high purity raw elements in an Ar-filled glovebox according to the stoichiometry. The ingot is obtained by applying an arc melting under Ar protection. Note that 3% addition Sb is added to compensate for the evaporation. During the intervals of the three-times melting, the sample is flipped over to guarantee the homogeneity. The arc-melted ingot is then powderized by the high energy ball milling (SPEX 8000D) for 2 hours. The obtained powder is sintered using the same SPS device but at 1473 K and 50 MPa for 3 mins. The sintering conditions are optimized to guarantee relative sample densities larger than 98%.

Sample Characterization

- **Microstructural Features**

Room-temperature X-ray diffraction patterns are measured in a Bruker D8 Advance diffractometer (Co radiation) to characterize the phases. A scanning electron microscope (SEM) is employed to characterize the morphology of sample surfaces that are either fine polished or freshly broken. Energy-dispersive X-ray spectroscopy (EDX) is employed to characterize the sample homogeneity and elemental ratio of selected compounds. The specimen for transmission electron microscope (TEM) investigations are prepared by traditional mechanical polishing, dimpling, and then ion milling with liquid nitrogen stage. Scanning TEM (STEM) imaging was carried out with JEOL ARM 200F equipped with double correctors.

- **ICP measurement**

The elemental ratios are additionally characterized by inductively coupled plasma optical emission spectrometry (ICP-OES; iCAP 6500 Duo View, Thermo Fisher Scientific) with a standard deviation of approximately 1% for each element. Three parallel weights of each sample about 30 mg are taken in a glove box. The materials are digested in a mixture of HNO₃ and HF at room temperature. The digestion solutions are filled up to 300 g. The final solutions for measurements have an acid concentration of 2% HNO₃ (65%) and 0.5% HF (40%). Every solution is measured four times.

- **Rietveld Refinement**

Selected samples for Rietveld refinement are hand milled by mortar and pestle. The powders are fixed between two acetate amorphous fine films by a glue that is a mixture of Amyl acetate and Collodion. The spectra are obtained by a STOE Stadi P Diffractometer with a Mo source and a Ge 111 Monochromator which yields a single wavelength of 0.7093 Å. For each sample, the scanning time is 7 to 8 hours for 2-Theta between 5° to 50°. The refinement is performed using Fullprof.

- **Sound velocity**

Samples with a size of $\sim 10 \times 10 \times 2$ mm³ are used for sound velocity measurements. The experiments are carried out by a RITEC Advanced Ultrasonic Measurement System

RAM-5000. The system realizes the pulse-echo method of time propagation measurements with an accuracy of about 10^{-3} μ s. To generate longitudinal (L) and shear (S) ultrasonic bulk waves, Olympus transducers V129-RM (10 MHz) and V157-RM (5 MHz) are used. Propylene glycol and SWC (Olympus) are used as couplant materials for L and S modes, respectively. Thickness measurements are carried out using Mitutoyo ID-HO530 device. All data are obtained at 300 K.

- **Thermoelectric Properties**

The electrical resistivity (ρ) and the Seebeck coefficient (S) are measured using a commercial device LSR-3 (Linseis). The thermal conductivity (K_{tot}) is calculated as a multiplication of thermal diffusivity (D), specific heat (c_p), and mass density (d) that are measured by laserflash (LFA1000, Linseis), differential scanning calorimetry (DSC 404, Netzsch), and an Archimedes kit, respectively. Carrier concentrations (n_H) are measured by a physical property measurement system (PPMS, Quantum Design) at room temperature using the Hall bar method under ± 3 T magnetic induction. The Hall mobility (μ_H) is calculated as $\mu_H = 1/\rho n_H e$. The measurement errors are 4%, 5%, and 12% for electrical resistivity, Seebeck coefficient, and thermal conductivity, respectively. Explicitly, the uncertainties of thermal conductivity originate from 2% in mass density, 4% in diffusivity, and 6% in specific heat. Therefore, the uncertainties in power factor and zT are 10% and 20%, respectively. To increase the readability of the graphs, we do not add the error bars on the curves.

***Ab initio* calculations based on density functional theory**

The formation energy of different defects and electronic calculations in this work are based on density functional theory (DFT) implemented in the Vienna Ab-initio Simulation Package (VASP)^{1, 2}. A supercell cell consisting of 27 ($3 \times 3 \times 3$) chemical units is adopted for structural relaxation and electron band calculations. The elements are represented by projector-augmented wave (PAW) potentials^{3, 4} with 350 eV energy cutoff and the 12 valence electrons for Zr ($4s^2 4p^6 5s^2 4d^2$); 9 for Co ($3d^7 4s^2$); 5 for Sb ($5s^2 5p^3$); and 4 for Sn ($5s^2 5p^2$) are treated explicitly. Initial relaxation and energetics are calculated *via* the generalized gradient approximation, Perdew–Burke–Ernzerhof (PBE)⁵. The first

Brillouin zone is sampled by the tetrahedron method on a gamma-centered $8 \times 8 \times 8$ k -mesh. All structures are relaxed until the force on each atom is less than 0.01 meV/Å. The defect formation energy, $\Delta H(q, \mu)$, as a function of charge state $q \in [-5, +5]$ and Fermi energy μ , is calculated using the standard supercell approach,⁶

$$\Delta H(q, \mu) = E^D - E^0 - \sum_i n_i \mu_i + q(\mu + E_V - \Delta V_{0/b}) + E_c^D \quad (\text{S1})$$

where $E^D - E^0$ is the difference in total energy between defective supercell and defect-free supercell, μ_i is the chemical potential for missing atoms i , n_i is the corresponding number of missing atoms. The electron chemical potential term, $q(\mu + E_V - \Delta V_{0/b})$, is calculated with the valence band maximum E_V , and potential alignment term $-\Delta V_{0/b}$ in the charge-neutral case. The last term E_c^D is the correction term, and is calculated by the approach developed by Freysoldt, Neugebauer, and Van de Walle⁷. In this work, we consider vacancies ($V_{\text{Zr}}, V_{\text{Co}}, V_{\text{Sb}}$), interstitials ($I_{\text{Zr}}, I_{\text{Co}}, I_{\text{Sb}}$) at the 4d sites, and Frenkel defects (only $V_{\text{Co}}-I_{\text{Co}}$ stable, other cases unstable). The elemental chemical potentials, μ_i ($i=\text{Zr}, \text{Co}, \text{Sb}$), are determined under the element-rich conditions where the chemical potentials of elemental metals (μ_{metal}) are employed to represent that of elemental atoms (μ_{atom}). For example, in calculating the total formation energy of Zr interstitials, I_{Zr} , we set the element-rich condition that $\mu_{\text{Zr}, \text{atom}} = \mu_{\text{Zr}, \text{metal}}$ in Equation S1. This is applied to all defect calculations.

Using density functional theory, we also calculated the dispersion relations and modal scattering rate. These require second-order and third-order interatomic force constants (IFCs), denoted by $\Phi_{\lambda, \lambda'}$ and $\Phi_{\lambda, \lambda, \lambda'}$. For this purpose, we applied the finite displacement technique implemented in Phonopy⁸ and Phono3py⁹, respectively. For the second-order IFC calculations, to construct the dynamical matrices, we displaced each atom by 0.01 Å in $3 \times 3 \times 3$ supercells (81 atoms). A Γ -centered $15 \times 15 \times 15$ k -mesh was used for Brillouin zone sampling. For the third-order IFC calculations, we used a $2 \times 2 \times 2$ supercell, atomic displacements of 0.03 Å, and a $45 \times 45 \times 45$ k -grid. For both second-order and third-order IFCs, we used density functional theory as described above for total

energy calculations. Given the third-order IFCs, the three-phonon scattering rate $1/\tau_\lambda$ can be formulated based on the Fermi's golden rule,

$$\begin{aligned} \frac{1}{\tau_\lambda} &= \frac{36\pi}{\hbar^2} \sum_{\lambda\lambda''} |\Phi_{\lambda\lambda\lambda''}|^2 \times \{ (n_\lambda^0 + n_{\lambda''}^0 + 1) \delta(\omega_\lambda - \omega_{\lambda'} - \omega_{\lambda''}) + (n_{\lambda'}^0 - n_{\lambda''}^0) [\delta(\omega_\lambda + \omega_{\lambda'} - \omega_{\lambda''}) - \delta(\omega_\lambda - \omega_{\lambda'} + \omega_{\lambda''})] \} \end{aligned} \quad (\text{S2})$$

where λ indicates phonon mode (q, j) , n^0 is the Bose-Einstein distribution, and the delta function $\delta(\cdot)$ enforces energy conservation during scattering. The formalism of Fermi's golden rule is consistent with the single-mode relaxation time approximation (RTA) of the Boltzmann equation. Both of these assume the single-particle transport picture. In the RTA, the lattice thermal conductivity can be defined as

$$\kappa = \frac{1}{V} \sum_{\lambda} C_{\lambda} v_{\lambda} \otimes v_{\lambda} \tau_{\lambda} \quad (\text{S3})$$

where V is the volume, $C_{\lambda} = k_B x \exp(x) / (\exp(x) - 1)$ is modal heat capacity, $x = \hbar\omega_{\lambda} / k_B T$, and v_{λ} and τ_{λ} are group velocity and relaxation time for mode λ . The group velocity could be obtained from phonon dispersion, and all the calculated results are presented in Section IV below.

In addition, the Grüneisen parameter for mode (q, ω) , $\gamma_{q\omega}$, is calculated by the finite difference method. Here \mathbf{q} is phonon wave vector and ω is energy. In terms of the dynamical matrix D_q , modal Grüneisen parameter is defined as

$$\gamma_{q\omega} = - \frac{V}{\omega_q} \frac{\partial \omega_q}{\partial V} = - \frac{V}{2\omega_q^2} \left\langle e_{q\omega} \left| \frac{\partial D_q}{\partial V} \right| e_{q\omega} \right\rangle \quad (\text{S4})$$

where V is the volume of a unit cell, $|e_{q\omega}\rangle$ is a phonon eigenvector. We calculate the phonon modes for three systems: equilibrium (V), compressed ($-V$), and expanded ($+V$), based on which central difference is used to approximate the $\partial D_q / \partial V$ operator,

$\partial D_q/\partial V \approx \Delta D_q/\Delta V$. The phonon modes are calculated with Phonopy and the perturbation in volume is made by a 3% change in lattice constant⁸.

II. Thermoelectric properties of $\text{ZrCoSb}_{1-x}\text{Sn}_x$

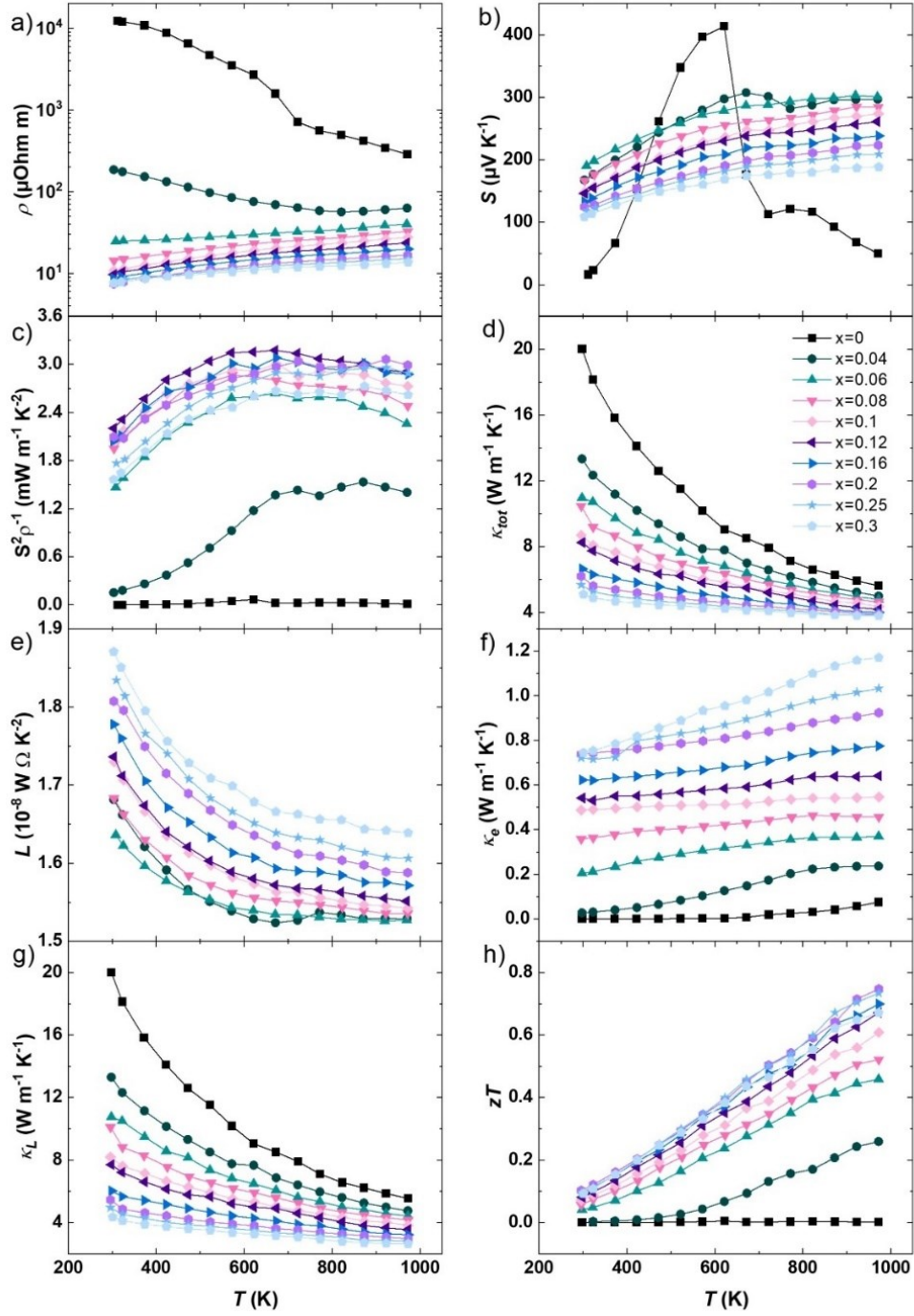


Figure S1. Temperature-dependent a) electrical resistivity, b) Seebeck coefficient, c) power factor, d) total thermal conductivity, e) Lorenz number, f) electronic thermal conductivity, g) lattice thermal conductivity, and h) zT of $\text{ZrCoSb}_{1-x}\text{Sn}_x$ where $x=0, 0.04, 0.06, 0.08, 0.1, 0.12, 0.16, 0.2, 0.25,$ and 0.3 .

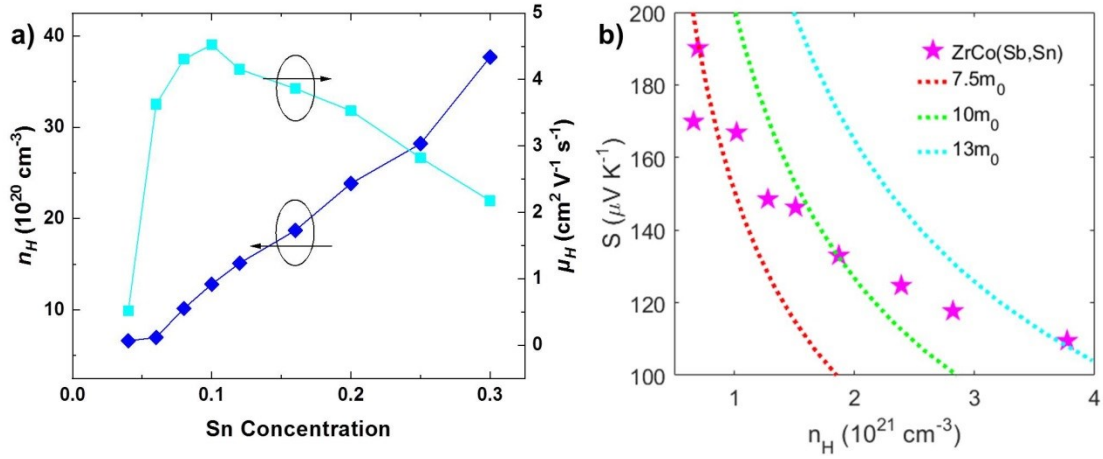


Figure S2. a) The carrier concentration (n_H) and carrier mobility (μ_H), and b) the Pisarenko plot of $\text{ZrCoSb}_{1-x}\text{Sn}_x$ at 300 K, where $x=0.04, 0.06, 0.08, 0.1, 0.12, 0.16, 0.2, 0.25,$ and 0.3 . The dotted line in b) suggests the corresponding density-of-states effective mass (m_{DOS}^*).

III. Anomalous reduction of κ_L in other half-Heusler compounds

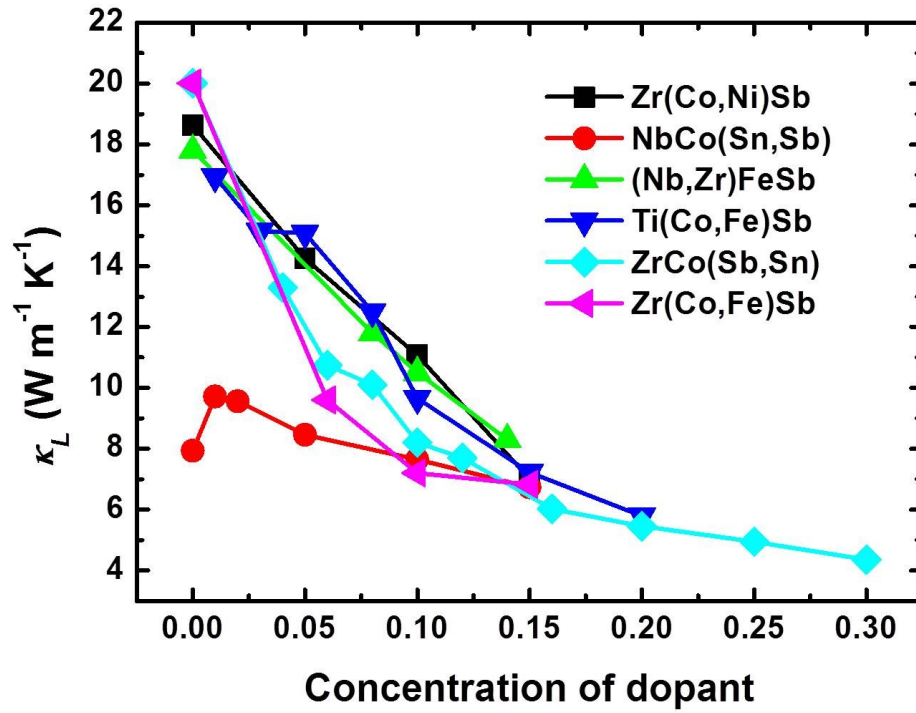


Figure S3. Anomalous κ_L reduction of a variety of half-Heusler compounds at 300 K including $\text{Zr}(\text{Co},\text{Ni})\text{Sb}$ ¹⁰, $\text{NbCo}(\text{Sn},\text{Sb})$ ¹¹, $(\text{Nb},\text{Zr})\text{FeSb}$ ¹², $\text{Ti}(\text{Co},\text{Fe})\text{Sb}$ ¹³, $\text{ZrCo}(\text{Sb},\text{Sn})$ (this work), and $\text{Zr}(\text{Co},\text{Fe})\text{Sb}$ (this work).

IV. Phonon dispersion and lattice thermal conductivity from first principles

With the methods detailed in Section I, We performed first-principle calculations for two compounds, ZrCoSb and ZrCoSb_{0.875}Sn_{0.125}. The calculated phonon dispersions, scattering rates, and group velocities are shown in Figure S4. Besides, the temperature-dependent calculated κ_L are shown in Figure S5 together with experimental κ_L of ZrCoSb and ZrCoSb_{0.88}Sn_{0.12}. Comparing the two materials in Figure S4, the dispersion relation change only negligibly due to Sn substitution. Besides, the change of group velocity is within 5%. Concerning the scattering rate, as expected, only the top-band optical modes are mostly influenced. Overall, doping 12.5% Sn on the Sb sites barely changed the dispersion or scattering rates of low-frequency modes.

Furthermore, although the substitution of Sn decreases κ_L both theoretically and experimentally, the reduction in κ_L show distinct behaviors in theory and experiments. In Figure R2b, we compare the temperature-dependent ratios of $\kappa_{L_Sn0.12}/\kappa_{L_ZrCoSb}$ by using either calculated or experimental κ_L from 250 K up to 1000 K. Based on the calculated results, we find that the of $\kappa_{L_Sn0.12}/\kappa_{L_ZrCoSb}$ ratio locates between 0.6 to 0.65 with minor variation within the calculation temperatures. This roughly-constant ratio of $\kappa_{L_Sn0.12}/\kappa_{L_ZrCoSb}$ is because of the dominant three-phonon process for both compounds that yields the $\kappa_L \sim T^{-1}$ relation. Moreover, using the experimental κ_L , the ratio of $\kappa_{L_Sn0.12}/\kappa_{L_ZrCoSb}$ is close to the calculation ones at temperatures higher than 750 K (the Green-shaded region in Figure R2b) since the phonon-phonon interaction dominates at high temperatures. On the other hand, the experimental ratio deviates from the calculation at lower temperatures (the Red-shaded region in Figure R2b), hindering the existence of another phonon scattering mechanism.

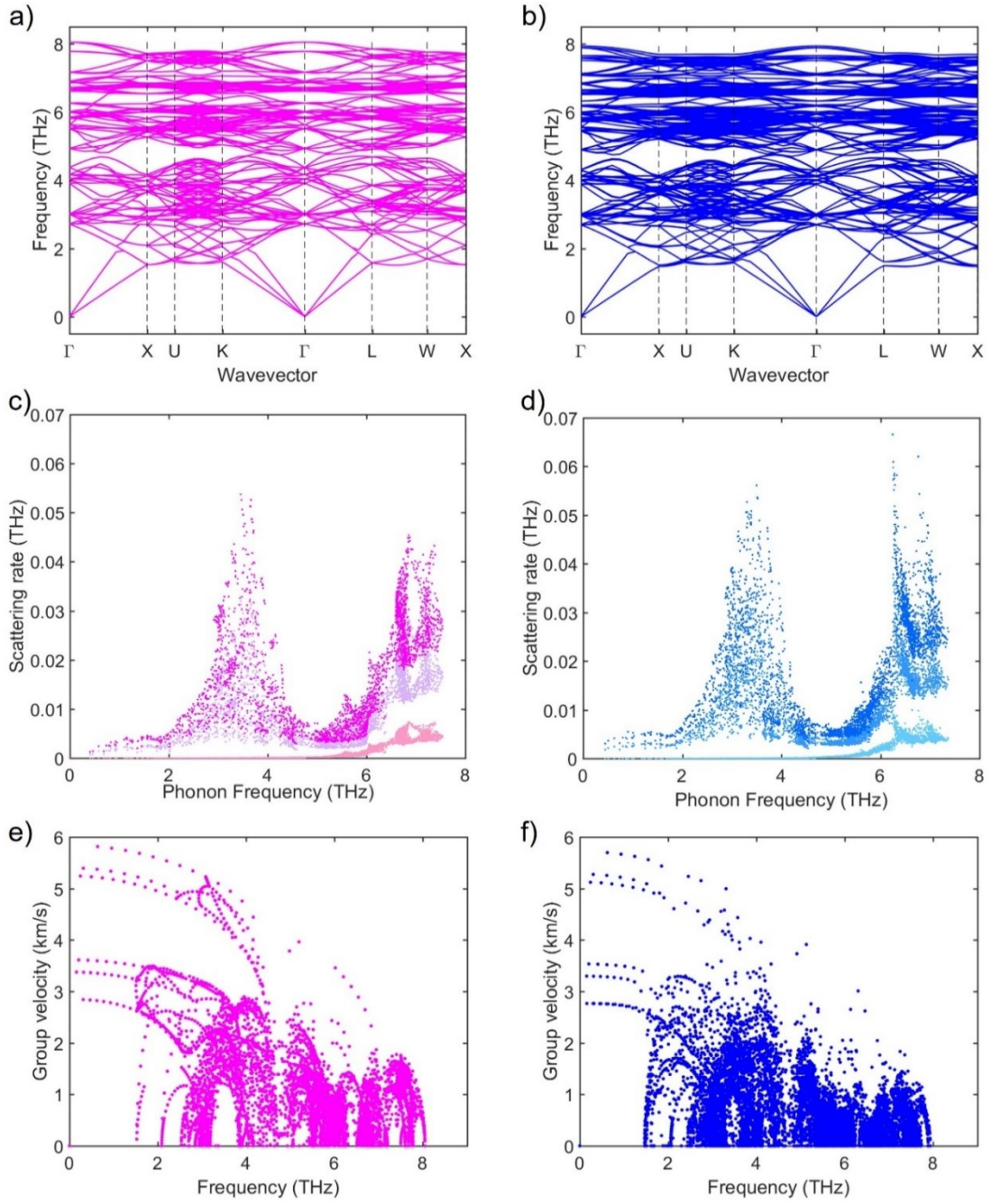


Figure S4. First-principle-calculation results of a) and b) phonon dispersion relations; c) and d) scattering rates; and e) and f) group velocities of ZrCoSb (a, c, e) and ZrCoSb_{0.875}Sn_{0.125} (b, d, f).

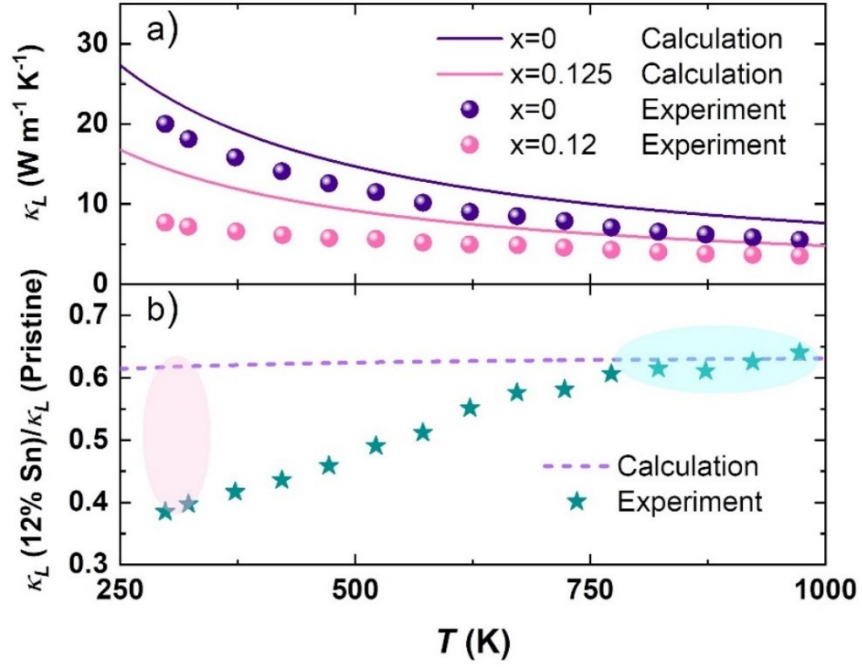


Figure S5. a) Comparison of temperature-dependent lattice-thermal-conductivity among the pristine ZrCoSb (from experiments and calculations), ZrCoSb_{0.875}Sb_{0.125} (from calculation), and ZrCoSb_{0.88}Sb_{0.12} (from experiments). b) The temperature-dependent ratios of $\kappa_{L_Sn0.12}/\kappa_{L_ZrCoSb}$ from experiments (star) or calculations (dotted line).

V. X-ray diffraction patterns

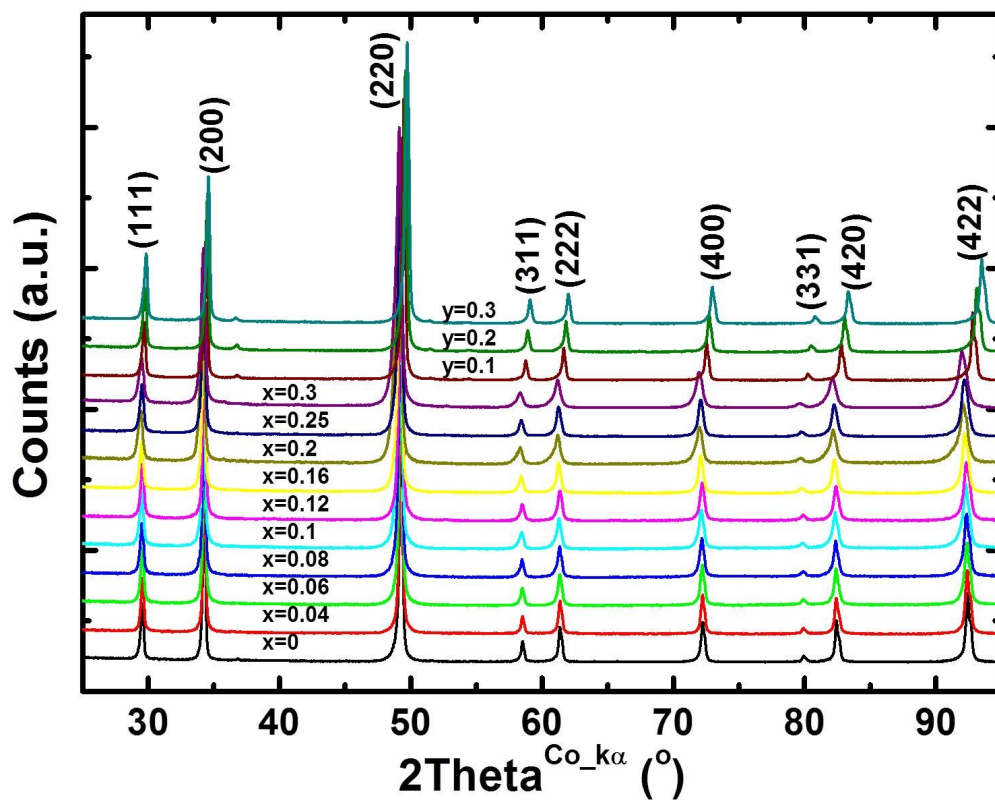


Figure S6. XRD of $\text{ZrCoSb}_{1-x}\text{Sn}_x$ and $\text{Zr}_{1-y}\text{Ti}_y\text{CoSb}$ with $x=0, 0.04, 0.06, 0.08, 0.1, 0.12, 0.16, 0.2, 0.25, 0.3$ and $y=0.1, 0.2, \text{ and } 0.3$.

VI. EDX mapping

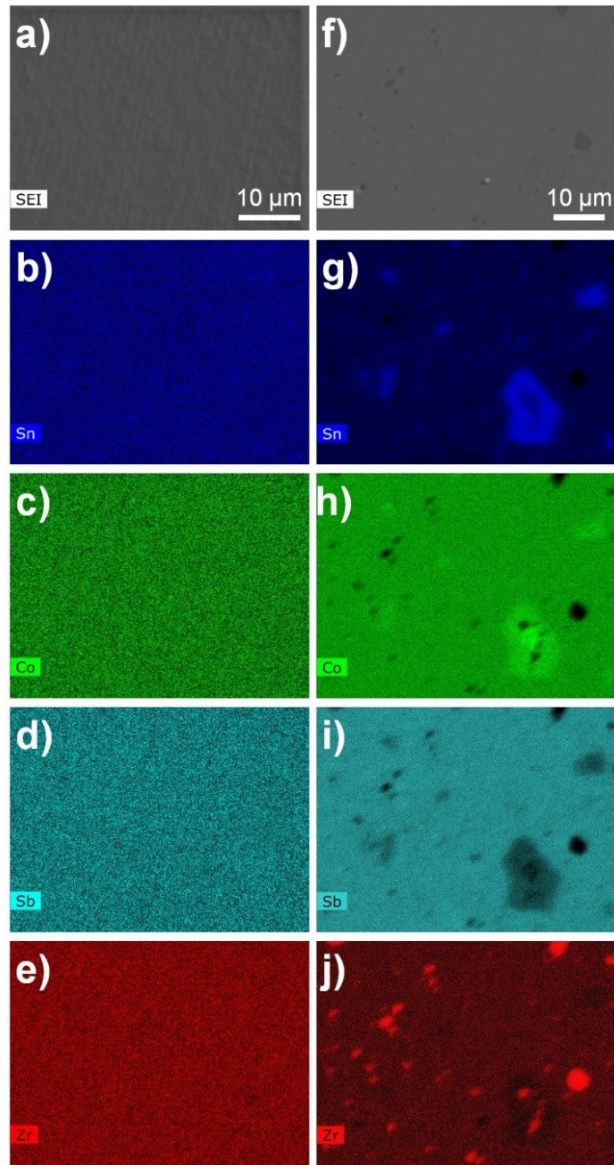


Figure S7. EDX mapping of $\text{ZrCoSb}_{0.8}\text{Sn}_{0.2}$, showing the secondary electron image (SEI, a and f) and the elemental distributions of Sn (b and g), Co (c and h), Sb (d and i), and Zr (e and j). The compounds are either synthesized by a long-termed ball milling (30 hours), following a current assisted sintering (a to e); or by using arc melting, following a short-term ball milling (2 hours), then the current assisted sintering (f to j). Uniform elemental distributions are observed for the compound that is long-term ball milled (a to e); meanwhile, obvious impurities such as elemental Zr and an unknown phase that is rich in Co and Sn are spotted in the other sample (f to j).

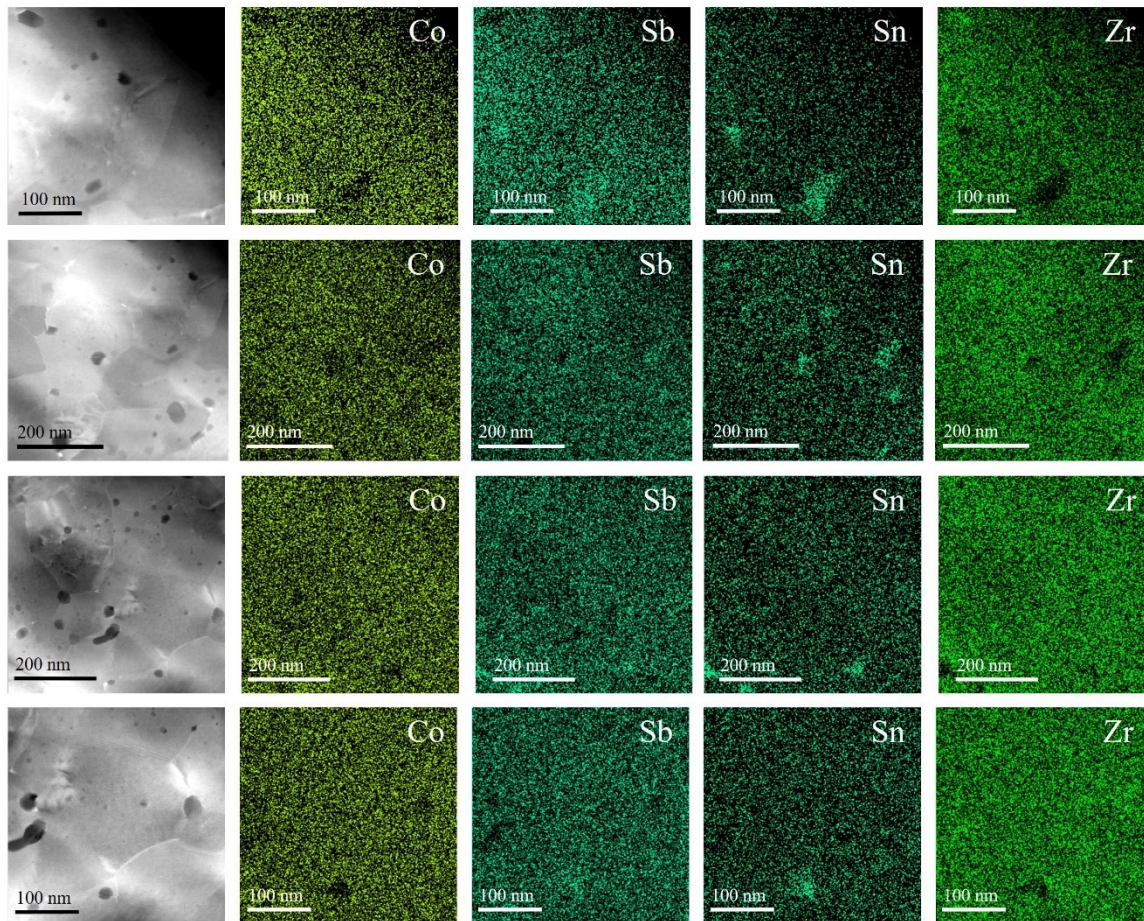


Figure S8. TEM images together with EDX mapping of $\text{ZrCoSb}_{0.7}\text{Sn}_{0.3}$.

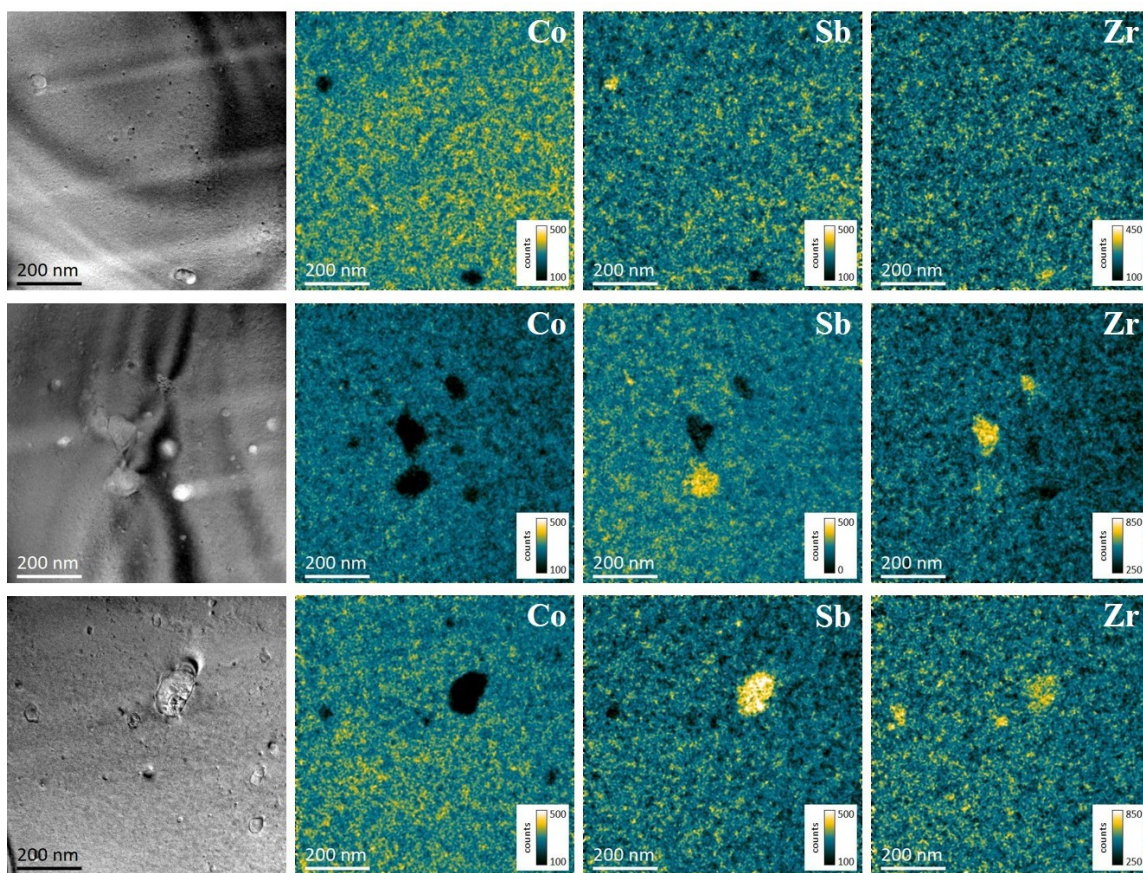


Figure S9. TEM images together with EDX mapping of ZrCoSb.

VII. Grain size distribution for selected compounds

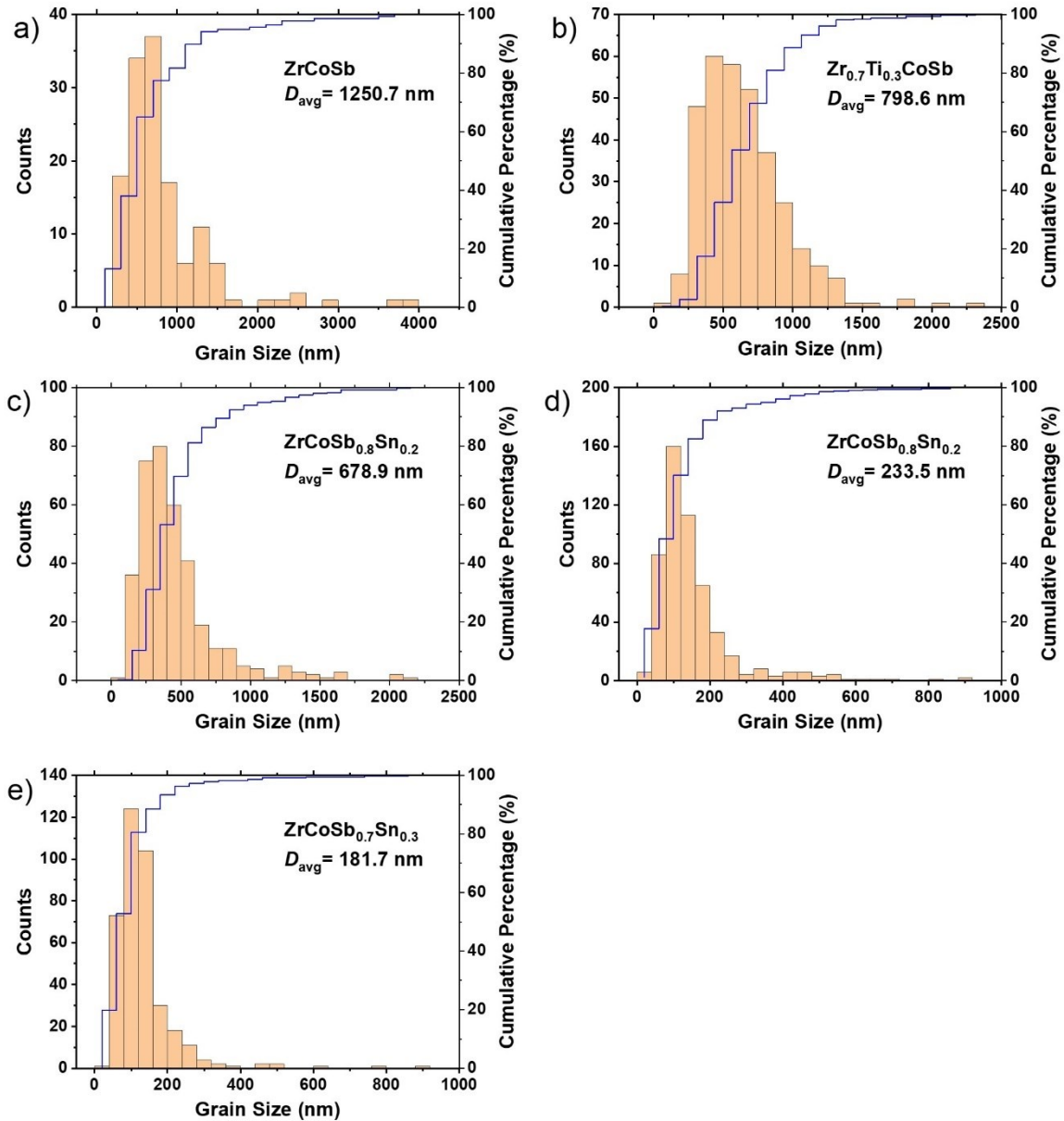


Figure S10. Statistical analysis of grain sizes by counts (bar, left axis) and cumulative percentage (blue line, right axis) of compounds a) ZrCoSb, b) $\text{Zr}_{0.7}\text{Ti}_{0.3}\text{CoSb}$, c) $\text{ZrCoSb}_{0.8}\text{Sn}_{0.2}$, d) $\text{ZrCoSb}_{0.8}\text{Sn}_{0.2}$, and e) $\text{ZrCoSb}_{0.7}\text{Sn}_{0.3}$. The enlarged grain size of $\text{ZrCoSb}_{0.8}\text{Sn}_{0.2}$ in c) is due to the modified sintering condition at 1473 K and 50 MPa for 30 mins, whereas the other compounds are sintered at 1323 K and 50 MPa for 3 mins. The area-weighted average grain sizes are also presented for each compound.

VIII. The BvK-Debye model details

In the BvK-Debye model, we apply the following assumptions,

- 1) The periodic boundary condition, *i.e.*, the Born-von Karman (BvK) boundary condition is applied instead of the acoustic-elastic-wave assumption that was used by Debye in 1912¹⁴. With the BvK boundary condition, the Debye dispersion is violated for phonons with wavevectors near the Brillouin zone boundary. The acoustic dispersion tends to be a sine-function instead of linear, as shown in Figures S11a and S11b. This dispersion was emphasized by Dames, *et al.*¹⁵, and the equations were given by Chen, *et al.*¹⁶,

$$\omega_{a,j}(k) = \frac{2}{\pi} v_{A,j} k_c \sin\left(\frac{\pi k}{2k_c}\right) \quad (\text{S5})$$

where the subscript a represents acoustic branches, j defines the polarization of lattice vibrations, and k_c is the cut-off frequency. We simplify the first Brillouin zone of a 3D solid as a sphere. Besides, acoustic branches are approximated as degenerate.

- 2) If the number of atoms in the primitive cell (N_{unit}) is one, then there is no optical branch and the whole dispersion is a sine function. However, N_{unit} is more than one for most materials (*e.g.*, $N_{unit} = 3$ for half-Heusler compounds). Therefore, the Brillouin zone is folded and the optical phonons appear. Typically, the heat-carrying optical phonons are approximated as a series of standing waves (*i.e.*, the Einstein oscillator) with a series of constant frequencies ($\omega_{o,i}$) (Figure S11c)¹⁷. According to Einstein's assumption, each of these optical modes possesses a minimum relaxation time, taken as half of its period.

$$\tau_{min, o,i} = \frac{\pi}{\omega_{o,i}} \quad (\text{S6})$$

This assumption, being employed by Chen, *et al.* together with the BvK dispersion, tends to underestimate the relaxation time of these modes as well as the optical thermal conductivity. Alternatively, as shown in Figure S11d, we apply a **Debye dispersion to these optical branches**. Thus, these optical phonons

obtain non-vanishing group velocities. Moreover, instead of assuming a minimum relaxation time (Equation S6), the scattering rate of these optical branches can be treated by the widely used Debye-Klemens model¹⁸. With the revised dispersion relation, we can assess the lattice thermal conductivity more accurately.

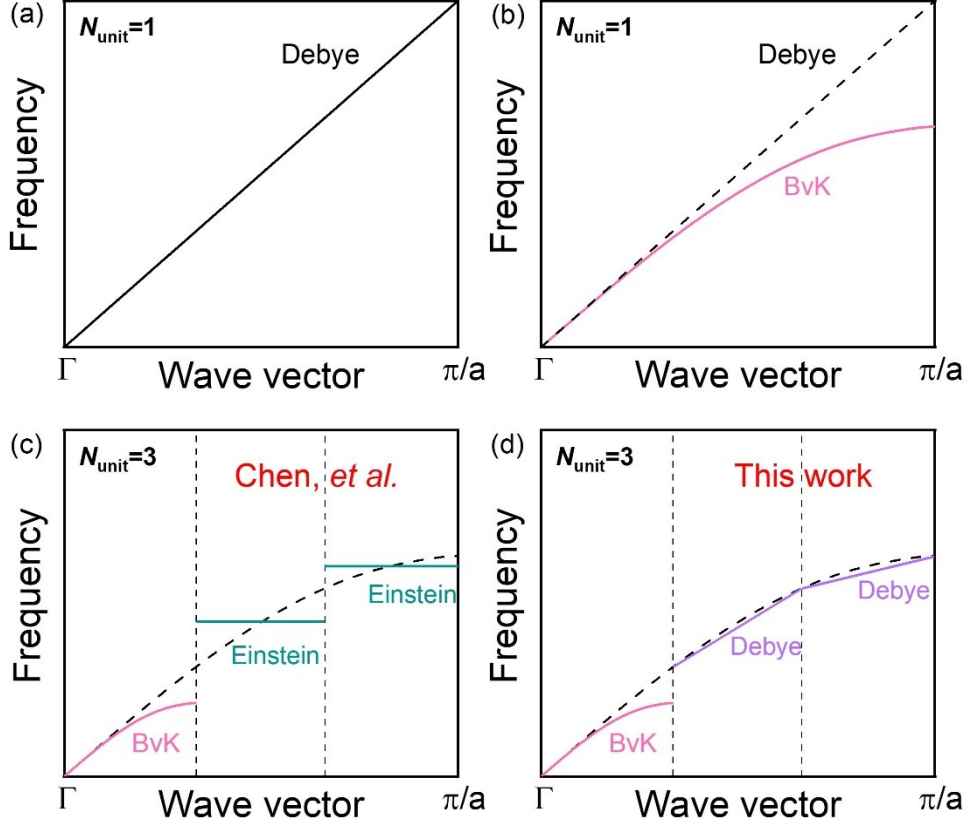


Figure S11. Schematics showing the phonon dispersions for the 1D atomic chain. (a) the Debye dispersion, (b) the BvK dispersion, (c) The BvK-Einstein dispersion (Chen, *et al.*)¹⁶, and (d) the BvK-Debye dispersion (this work).

- 3) Specifically, for the grain boundary scattering, usually the “grey” model, *i.e.*, a frequency-independent scattering rate was applied,

$$\tau_{GB}^{-1} = v_A/D \quad (S7)$$

This treatment has been widely used due to its simplicity and high accuracy at higher temperatures. However, a previous work of Wang, *et al.* observed a $\kappa_L \sim T^2$ relation for nanocrystalline silicon at lower temperatures, which violates the

$\kappa_L \sim T^3$ variation that was predicted in the grey model¹⁹. The inconsistency was alleviated by considering a “non-grey” model where the scattering rate become frequency-dependent,

$$\tau_{GB}^{-1} \sim C\omega \quad (S8)$$

With the non-grey model, Wang, *et al.* reproduced the $\kappa_L \sim T^2$ relation at lower temperatures but with fitting parameter (the pre-factor C in Equation S8). Further, the frequency dependence in the non-gray model was rationalized by Kim, *et al.* by treating grain boundary as a collection of dislocations²⁰. Then phonon scattering by grain boundaries was considered as scattering by dislocation cores (DC) and dislocation strains (DS),

$$\tau_{DC}^{-1} = N_D \frac{V^{4/3}}{v_A^2} \omega^3 \quad (S9)$$

$$\tau_{DS}^{-1} = 0.6 \times B_{eff}^2 N_D \gamma^2 \left\{ \frac{1}{2} + \frac{1}{24} \left(\frac{1-2r}{1-r} \right)^2 \times \left[1 + \sqrt{2} \left(\frac{v_L}{v_S} \right)^2 \right]^2 \right\} \omega \quad (S10)$$

N_D is the dislocation density, B_{eff} is the effective Burgers vector, and r is the Poisson's ratio. Note that phonon scattering rates by dislocation core and dislocation strain follow the ω^3 and ω relations, respectively. Nevertheless, the scattering intensity from dislocation strain is usually much stronger than dislocation cores²¹, thus yielding a $\tau_{GB}^{-1} \sim \omega$ relation, *i.e.*, $\tau_{GB}^{-1} \approx \tau_{DS}^{-1}$.

Accordingly, we employ the non-grey model to evaluate the boundary scattering. The density of dislocation can be estimated from the grain size through²²,

$$N_D = \frac{\sqrt{12} \times \varepsilon}{D \times B_{eff}} \quad (S11)$$

D is the area-weighted average grain size. The strain, ε , is obtained from the powder XRD pattern following the Williamson-Hall plot²³. The norm of the

Burgers vector (B_{eff}) for *fcc* lattice is usually calculated from the lattice parameter (a),

$$B_{eff} = \frac{a}{2} \langle 110 \rangle = \frac{a}{2} (1^2 + 1^2 + 0^2)^{0.5} = \frac{a}{\sqrt{2}} \quad (S12)$$

The equations for the BvK-Debye modeling are given as follows:

- The **acoustic** branch follows Chen, *et al.*¹⁶,

The average sound velocity (v_A) is calculated based on the speeds of the longitudinal (v_L) and shear mode (v_s),

$$\frac{1}{v_A^3} = \frac{1}{3} \left(\frac{1}{v_L^3} + \frac{2}{v_s^3} \right) \quad (S13)$$

The Poisson's ratio r ,

$$r = \frac{1 - 2(v_s/v_L)^2}{2 - 2(v_s/v_L)^2} \quad (S14)$$

The Grüneisen parameter γ ,

$$\gamma = \frac{3}{2} \left(\frac{1+r}{2-3r} \right) \quad (S15)$$

The cut-off wave vector of the acoustic branch q_a ,

$$q_a = \left(\frac{6\pi^2}{VN_{unit}} \right)^{\frac{1}{3}} \quad (S16)$$

where V is the average volumetric occupation of each atom in the lattice (not the volume of the atom itself), N_{unit} is 3 for half-Heusler compounds.

$$V = \bar{M}/d \quad (S17)$$

\bar{M} is the average atomic mass, d is the mass density.

Accordingly, the cut-off frequency (ω^D) is given by,

$$\omega_D = \frac{2}{\pi} v_A q_a \quad (\text{S18})$$

The effective ‘‘Debye temperature’’ of the acoustic branch ($\theta_{D, a}$),

$$\theta_{D, a} = \frac{\hbar}{k_B} \omega_D \quad (\text{S19})$$

With the sine-dispersion, the frequency-dependent group velocity is v_g ,

$$v_g = v_A \sqrt{1 - \left(\frac{T * x}{\theta_{D, a}} \right)^2} \quad (\text{S20})$$

The frequency-dependent phase velocity v_p ,

$$v_p = \frac{x}{\frac{2}{\pi} * q_a * \arcsin\left(\frac{T * x}{\theta_{D, a}}\right)} * \frac{k_B T}{\hbar} \quad (\text{S21})$$

where x is the reduced frequency,

$$x = \frac{\hbar \omega}{k_B T} \quad (\text{S22})$$

The relaxation time of the phonon-phonon interaction is τ_{PP} ,

$$\tau_{PP}^{-1} = \left(\frac{k_B T}{\hbar} \right)^2 \frac{2k_B V^{1/3} \gamma^2 T}{M v_p^2 v_g} x^2 \quad (\text{S23})$$

The relaxation time of the grain boundary scattering (τ_{GB}) follows Equations S9 to S12.

The relaxation time of the point defect scattering (τ_{PD}) will be discussed later in section XIII.

The total relaxation time follows the Matthiessen’s rule,

$$\tau_{eff}^{-1} = \tau_{PP}^{-1} + \tau_{GB}^{-1} + \tau_{PD}^{-1} + \dots \quad (\text{S24})$$

The lattice thermal conductivity from the acoustic branch is calculated as,

$$\kappa_{L,a} = \int_0^{\theta_D} v_g^2 * \tau_{eff} * \frac{k_B x^2}{2\pi^2 v_p^2 v_g} \left(\frac{k_B T}{\hbar} \right)^3 * \frac{x^2 e^x}{(e^x - 1)^2} dx \quad (\text{S25})$$

- The **optical** branches are evaluated in the following way,

Note that transverse and longitudinal modes are **degenerated**, therefore, we consider only 2 (instead of 6) optical branches for half-Heusler compounds. We name the lower-frequency optical branch as the “first” optical phonon, whereas the higher-frequency optical branch is called the “second” optical phonon.

The lower cut-off wavevector of the first optical branch $q_{o1,-}$,

$$q_{o1,-} = \left(\frac{6\pi^2}{VN_{unit}} \right)^{\frac{1}{3}} = q_a \quad (\text{S26})$$

The upper cut-off wavevector of the first optical branch $q_{o1,+}$,

$$q_{o1,+} = \left(\frac{6\pi^2}{V(N_{unit} - 1)} \right)^{\frac{1}{3}} \quad (\text{S27})$$

The lower cut-off wavevector of the second optical branch $q_{o2,-}$,

$$q_{o2,-} = q_{o1,+} = \left(\frac{6\pi^2}{V(N_{unit} - 1)} \right)^{\frac{1}{3}} \quad (\text{S28})$$

The upper cut-off wavevector of the second optical branch $q_{o2,+}$,

$$q_{o2,+} = \left(\frac{6\pi^2}{V(N_{unit} - 2)} \right)^{\frac{1}{3}} \quad (\text{S29})$$

The upper cut-off frequency of the second optical branch $\omega_{o2,+}$,

$$\omega_{o2,+} = \frac{2}{\pi} v_A q_{o2,+} \quad (\text{S30})$$

The lower cut-off frequency of the second optical branch $\omega_{o2,-}$,

$$\omega_{o2,-} = \omega_{o2,+} \sin\left(\frac{\pi q_{o2,-}}{2q_{o2,+}}\right) \quad (\text{S31})$$

The upper cut-off frequency of the first optical branch $\omega_{o1,+}$,

$$\omega_{o1,+} = \omega_{o2,+} \sin\left(\frac{\pi q_{o1,+}}{2q_{o2,+}}\right) \quad (\text{S32})$$

The lower cut-off frequency of the first optical branch $\omega_{o1,-}$,

$$\omega_{o1,-} = \omega_{o2,+} \sin\left(\frac{\pi q_{o1,-}}{2q_{o2,+}}\right) \quad (\text{S33})$$

The effective group velocity of the first optical branch ($v_{g,o1}$)

$$v_{g,o1} = \frac{\omega_{o1,+} - \omega_{o1,-}}{q_{o1,+} - q_{o1,-}} \quad (\text{S34})$$

The effective group velocity of the second optical branch ($v_{g,o2}$)

$$v_{g,o2} = \frac{\omega_{o2,+} - \omega_{o2,-}}{q_{o2,+} - q_{o2,-}} \quad (\text{S35})$$

The effective ‘‘Debye temperature’’ of the first optical branch ($\theta_{D,o1}$),

$$\theta_{D,o1} = \frac{\hbar}{k_B} \omega_{o1,+} \quad (\text{S36})$$

The effective ‘‘Debye temperature’’ of the second optical branch ($\theta_{D,o2}$),

$$\theta_{D,o2} = \frac{\hbar}{k_B} \omega_{o2,+} \quad (\text{S37})$$

The lattice thermal conductivity from the first optical branch ($\kappa_{L,o1}$) can be evaluated within the Debye-Klemens model¹⁸,

$$\kappa_{L,o1} = \frac{k_B}{2\pi^2 v_{g,o1}} \left(\frac{k_B}{\hbar}\right)^3 T^3 \int_{\hbar\omega_{o1,-}/k_B T}^{\hbar\omega_{o1,+}/k_B T} \tau_{eff} \frac{x^4 e^x}{(e^x - 1)^2} dx \quad (S38)$$

Similarly, the lattice thermal conductivity from the second optical branch ($\kappa_{L,o2}$),

$$\kappa_{L,o2} = \frac{k_B}{2\pi^2 v_{g,o2}} \left(\frac{k_B}{\hbar}\right)^3 T^3 \int_{\hbar\omega_{o2,-}/k_B T}^{\hbar\omega_{o2,+}/k_B T} \tau_{eff} \frac{x^4 e^x}{(e^x - 1)^2} dx \quad (S39)$$

The total relaxation time follows the Matthiessen's rule,

$$\tau_{eff}^{-1} = \tau_{PP_o}^{-1} + \tau_{GB}^{-1} + \tau_{PD}^{-1} + \dots \quad (S40)$$

Since the dispersion relation is assumed as linear for optical branches, a different expression of the phonon-phonon interaction relaxation time applies²⁴,

$$\tau_{PP_o1}^{-1} = \frac{4\pi k_B \gamma_1^2 V^{1/3}}{\sqrt{2} M v_{g,o1}^3} T \omega^2 \quad (S41)$$

$$\tau_{PP_o2}^{-1} = \frac{4\pi k_B \gamma_1^2 V^{1/3}}{\sqrt{2} M v_{g,o2}^3} T \omega^2 \quad (S42)$$

γ_1 is the reduced Grüneisen parameter and $\gamma_1 = \frac{1}{\sqrt{N}} \gamma$, where N is the number of atoms in the conventional unit cell²⁵, for half-Heusler $N=12$.

The relaxation time from grain boundaries (τ_{GB}) and point defects (τ_{PD}) are treated identically as of the acoustic branch.

IX. Electron-phonon interaction intensity of ZrCoSb, NbFeSb, and ZrCoBi

Under the framework of the Debye-Klemens model, the intrinsic three-phonon process can be considered as the “background” of the scattering profile, of which the relaxation time is determined by Equations S23, S41, and S42. According to a previous report, we consider ZrCoBi possessing a stronger phonon-phonon interaction than ZrCoSb and NbFeSb; meanwhile, the phonon-phonon interaction intensities between ZrCoSb and NbFeSb should be similar due to their similar thermal conductivities from room temperature up to 973 K²⁶.

For comparing the scattering intensity from the charge carriers, we consider the phonon relaxation time (τ_{EP}) of acoustic branches at higher temperatures²⁷,

$$\tau_{EP}^{-1}(\omega) = \frac{(2\pi m^*)^{1/2} E_{def}^2}{(k_B T)^{3/2} N_V d v_A} \exp\left(-\frac{m_{DOS}^* v_A^2}{2k_B T}\right) n_H \omega \quad (\text{S43})$$

where m_{DOS}^* is the density-of-state effective mass, E_{def} is the deformation potential, N_V is the valley degeneracy, which can be counted from the electron band structure, d is the sample density, and ω is the phonon frequency. E_{def} can be evaluated as²⁸,

$$\mu_0 = \frac{2\sqrt{2}e\pi\hbar^4 v_L^2 D}{3(k_B T)^{3/2} E_{def}^2 (m_{DOS}^*)^{5/2}} \quad (\text{S44})$$

$$\mu_H = \frac{F_0(\eta)}{2F_{1/2}(\eta)} \mu_0 \quad (\text{S45})$$

where μ_H is the Hall mobility, $F_n(\eta)$ is the Fermi integral of order n ,

$$F_n(\eta) = \int_0^\infty \frac{\chi^n}{1 + e^{\chi - \eta}} d\chi \quad (\text{S46})$$

η is the reduced Fermi level, which can be evaluated from the Seebeck coefficient,

$$S = + \left(\frac{k_B}{e}\right) \left[\frac{2F_1(\eta)}{F_0(\eta)} - \eta \right] \quad (\text{S47})$$

The related parameters are presented in Table S1, from which we evaluate the EP interaction intensities and find that ZrCoSb has a scattering rate similar to ZrCoBi, but larger than NbFeSb by roughly 3 times. Since the EP interaction is already insignificant for the κ_L reduction of ZrCoSb, it is less likely to yield effective phonon scattering in ZrCoBi and NbFeSb. Our comparison study suggests that the EP interaction contributes insignificantly to the phonon scattering of the ZrCoSb-, the NbFeSb-, the ZrCoBi- and possibly the ZrNiSn-based half-Heusler compounds²⁹.

Table S1. Some important parameters for the phonon relaxation times. Three compositions, ZrCoSb_{0.9}Sn_{0.1}, Nb_{0.92}Zr_{0.08}FeSb, and ZrCoBi_{0.9}Sn_{0.1}, are specifically selected to compare the EP interaction intensity due to their similar carrier concentrations.

Parameters	ZrCoSb _{0.9} Sn _{0.1}	Nb _{0.92} Zr _{0.08} FeSb	ZrCoBi _{0.9} Sn _{0.1}
n_H (10^{21} cm ⁻³)	1.25	1.21	1.46
γ	1.55	1.7	1.61
N_V	8	8	10
d (g cm ⁻³)	8.01	8.46	9.6
v_A (m s ⁻¹)	3582	3438	2747
E_{def} (eV)	20.9	12.1	17.6
m^* (m_0)	8.7	7.5	10.7

X. Low-magnification TEM images

We perform a low-magnification TEM study of $\text{ZrCoSb}_{0.7}\text{Sn}_{0.3}$. Figure S12 displays some representative TEM images that are taken at randomly selected regions, showing the uniformity of morphology throughout the compound. Besides, it reveals that the sample is well crystallized with a grain size in the order of ~ 200 nm, similar to the SEM results. Besides, the concentrations of some other defects such as dislocations and precipitates are small, indicating their negligible contribution to the reduction of κ_L .

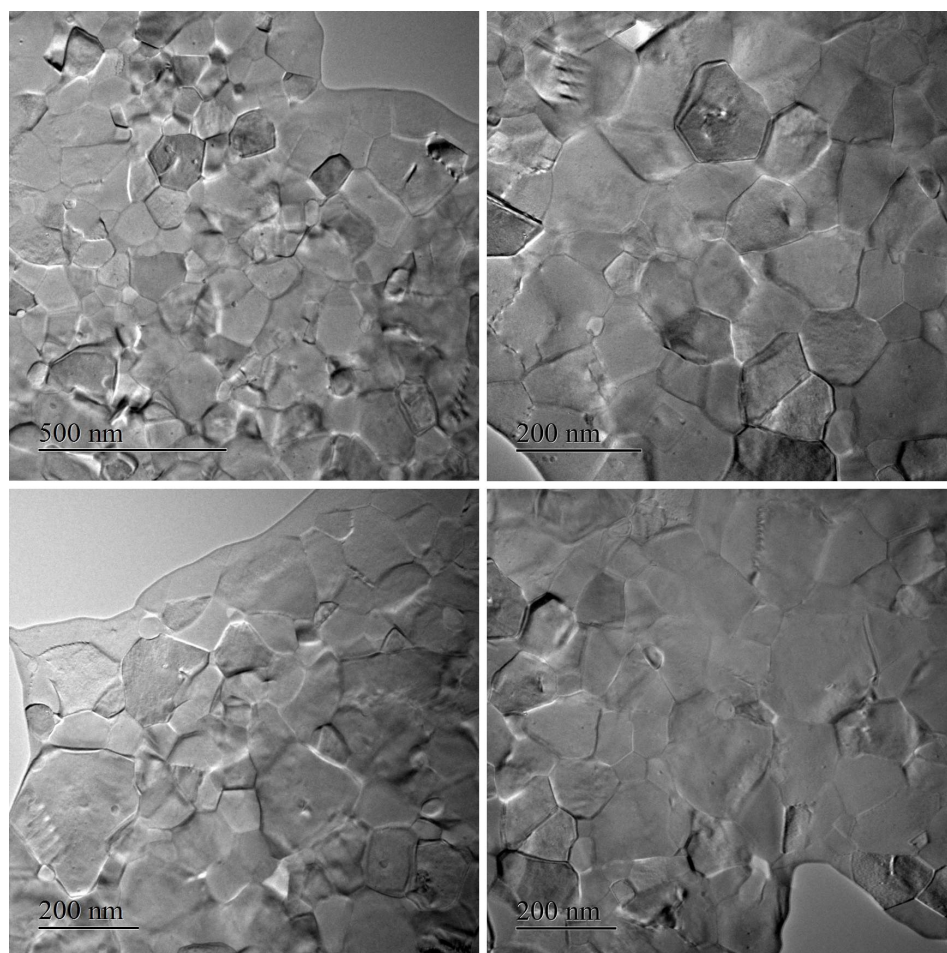


Figure S12. Low-resolution TEM images of $\text{ZrCoSb}_{0.7}\text{Sn}_{0.3}$.

XI. Elemental ratios

Table S2. Mass ratio of $\text{ZrCoSb}_{0.8}\text{Sn}_{0.2}$, ZrCoSb , and $\text{Zr}_{0.8}\text{Ti}_{0.2}\text{CoSb}$ determined by ICP

	Zr	Ti	Co	Sb	Sn
$\text{ZrCoSb}_{0.8}\text{Sn}_{0.2}$	33.83 (0.32)	--	21.50 (0.18)	35.54 (0.35)	8.68 (0.06)
ZrCoSb	33.50 (0.18)	--	22.27 (0.09)	44.62 (0.25)	--

Zr_{0.8}Ti_{0.2}CoSb 27.68 (0.34) 3.64 (0.05) 22.04 (0.24) 46.03 (0.57) --

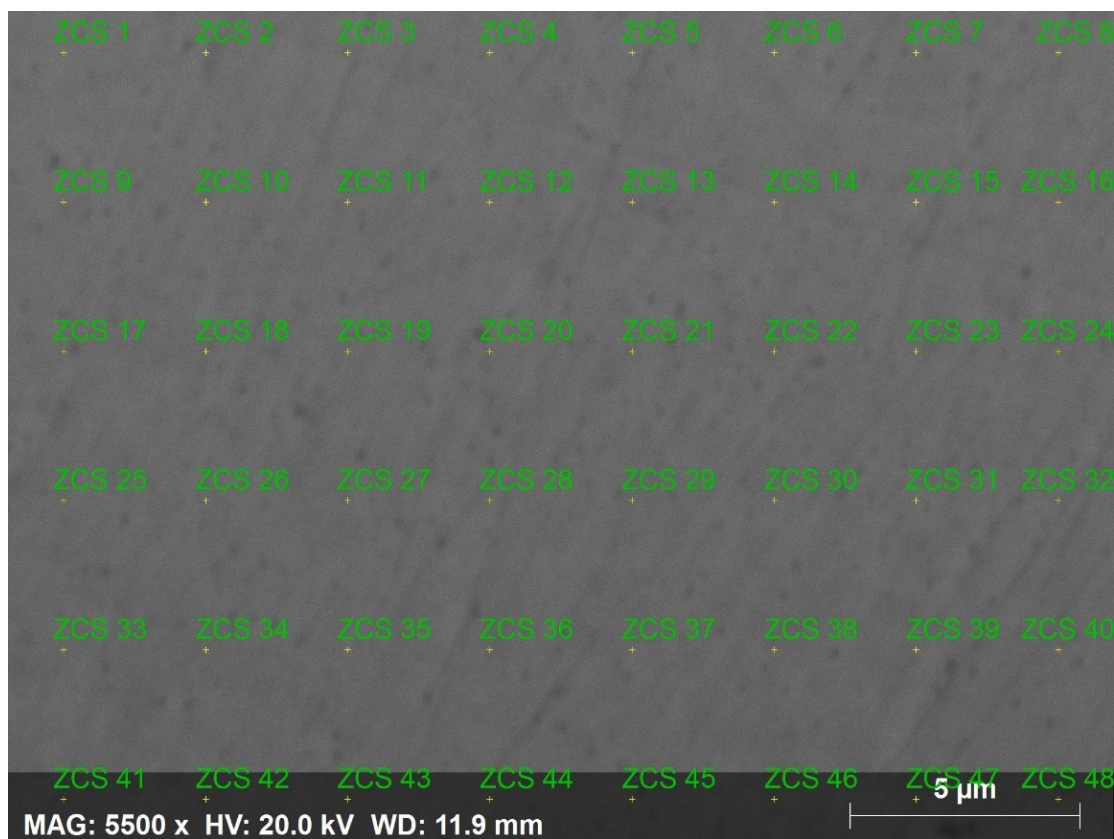


Figure S13. SEM image of the polished surface of ZrCoSb_{0.7}Sn_{0.3}. The markers show the positions of EDX measurement.

Table S3. EDX compositions of ZrCoSb_{0.7}Sn_{0.3}, the positions are shown in Figure S13.

Position	Co	Zr	Sn	Sb
1	33.69	34.69	9.05	22.58
2	33.36	32.87	9.74	24.04
3	33.09	34.89	9.27	22.74
4	33.91	32.77	9.59	23.73
5	33.45	32.82	9.92	23.82
6	33.26	33.61	9.47	23.65
7	33.68	33.79	9.25	23.28
8	33.08	34.74	8.97	23.21

9	33.03	34.85	9.11	23.01
10	33.40	33.90	9.65	23.06
11	33.60	32.65	9.73	24.02
12	33.09	35.48	8.82	22.61
13	33.58	34.42	9.05	22.96
14	32.96	34.08	9.23	23.73
15	33.32	32.98	9.74	23.97
16	33.66	32.44	9.79	24.11
17	33.92	35.13	8.52	22.43
18	33.42	34.65	9.05	22.88
19	33.36	33.43	9.33	23.88
20	34.00	33.99	9.02	22.99
21	33.48	33.13	9.89	23.50
22	33.11	34.92	9.22	22.74
23	33.56	35.48	9.10	21.86
24	33.71	34.80	8.63	22.86
25	33.57	33.88	9.49	23.06
26	32.82	34.90	9.56	22.71
27	33.46	33.55	9.53	23.46
28	33.05	35.70	9.07	22.19
29	33.59	34.52	9.16	22.72
30	33.56	32.76	10.08	23.60
31	33.13	33.52	9.75	23.60
32	33.30	33.87	9.38	23.45
33	33.96	33.04	9.77	23.23
34	32.90	34.69	9.33	23.08
35	33.68	33.20	9.63	23.49
36	32.81	35.62	9.12	22.45
37	33.57	33.02	9.61	23.81
38	32.93	35.64	8.97	22.46
39	33.31	33.22	10.17	23.30
40	33.39	33.07	9.84	23.71
41	33.32	33.18	10.05	23.45
42	33.00	33.52	9.91	23.58
43	32.87	33.50	9.45	24.17
44	33.02	35.44	8.98	22.56
45	33.36	33.54	9.91	23.19
46	33.28	34.86	8.96	22.90
47	33.27	33.56	9.61	23.57
48	33.01	36.06	8.76	22.16
<i>Mean</i>	33.34	34.05	9.68	22.93
<i>s.d.</i>	0.30	0.97	1.86	2.13

XII. Rietveld refinement

Figure S14 shows the refinement patterns of $\text{ZrCoSb}_{0.8}\text{Sn}_{0.2}$ with or without including the Co/4d Frenkel defects. The refinement quality factors are given in Table 3 in the main text.

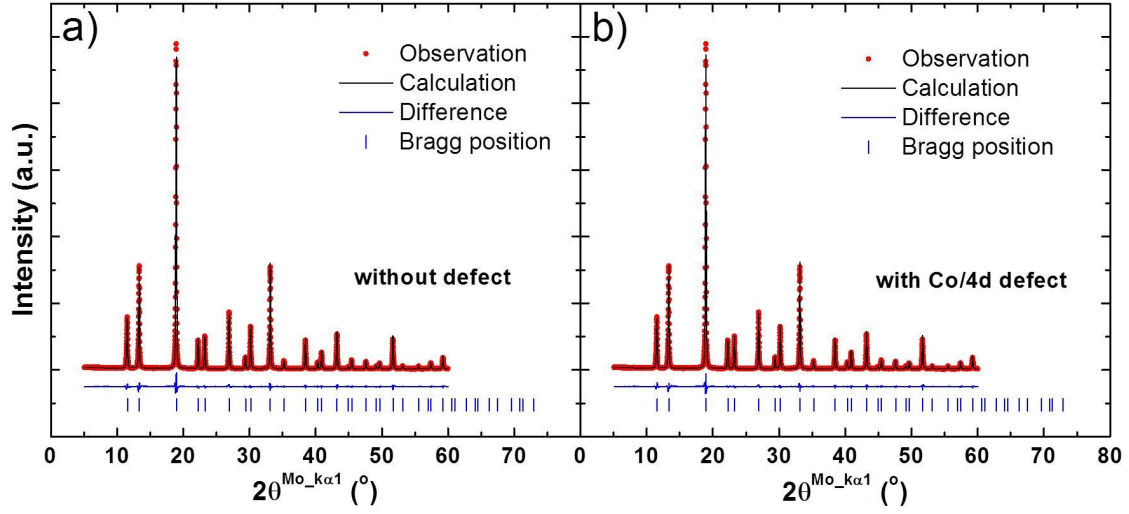


Figure S14. The Rietveld refinement of $\text{ZrCoSb}_{0.8}\text{Sn}_{0.2}$ a) without and b) with Co/4d Frenkel defects.

XIII. Co/4d Frenkel defects for κ_L reduction

We investigate the effect of Co/4d Frenkel defects for κ_L reduction under the framework of the BvK-Debye model. The point defect scattering the phonon relaxation time (τ_{PD}) is,

$$\tau_{PD}^{-1} = \frac{V}{4\pi v_p^2 v_g} \Gamma \omega^4 \quad (\text{S48})$$

where Γ , the scattering parameter, is related to the types and quantities of point defects. It is generally defined as^{30, 31},

$$\Gamma = \frac{1}{3} \left(\frac{\bar{m}}{\bar{M}} \right)^2 \left[\sum_i f_i \left(1 - \frac{m_i}{\bar{m}} \right)^2 + \epsilon \sum_i f_i \left(1 - \frac{r_i}{\bar{r}} \right)^2 \right] \quad (\text{S49})$$

The two terms in the bracket of Equation S49 correspond to the fluctuations of mass and radius due to the point defects, respectively, and they represent the perturbations of the lattice Hamiltonian from the kinetic energy and the potential energy, respectively. \bar{M} is the average atomic mass. \bar{m} and \bar{r} are the average atomic mass and average radius of the substituted sites, respectively. f_i , m_i , and r_i are the fractional concentration, atomic mass, and atomic radius of the i -th substitution atom, respectively, and ϵ is a phenomenological parameter for fitting, which is usually between 10 to 200. The term $\frac{1}{3}$ is included since there are three atoms in the primitive cell of the half-Heusler compounds. The scattering parameter Γ is addable from defects at different lattice sites.

Firstly, assume that the Co/4d Frenkel defects are absent, and phonon scattering mainly originates from the contrasts in the mass and the (covalence) radius between Sb (138 pm) and Sn (141 pm). In this case, we find that the fitting parameter, ϵ , has to reach ~ 1500 to match the experimentally reduced κ_L . Such an immense ϵ is unphysical, suggesting that phonon reduction should not originate from the Sb/Sn substitutional defect.

Contrarily, under the presence of vacancy point defects, the lattice Hamiltonian is modified by a kinetic energy term due to the missed vibration of atomic mass (T'), as well as by a doubled potential energy term due to the removal of bonding ($2U'$). Furthermore, the perturbations from the kinetic energy and the potential energy can be combined into a single term according to the virial theorem ($T' = U'$)³², thus the scattering parameter is,

$$\Gamma_{vac} = \frac{1}{3} \left(\frac{1}{\bar{M}} \right)^2 [f_i (-m_{vac} - 2\bar{M})^2] \quad (\text{S50})$$

where m_{vac} is the mass of the vacant atom, and f_i is the concentration of vacancies. This way the fitting parameter ϵ is removed. Similarly, for scattering by interstitials with mass m_{int} , the scattering parameter is³³,

$$\Gamma_{int} = \frac{1}{3} \left(\frac{1}{\bar{M}} \right)^2 [f_i (m_{int} + 2\bar{M})^2] \quad (\text{S51})$$

The total scattering parameter is addable from different point defects, therefore, for Frenkel defects, we have

$$\Gamma = \Gamma_{vac} + \Gamma_{int} \quad (\text{S52})$$

To match up to the experimental K_L , the calculated concentrations of Co/4d Frenkel defects are 2.5% and 3.3% for $\text{ZrCoSb}_{0.8}\text{Sn}_{0.2}$ and $\text{ZrCoSb}_{0.7}\text{Sn}_{0.3}$, respectively, which are similar to the ones that are determined from other approaches.

XIV. The impact of Co/4d defects on the electronic transport properties

Based on our calculation results from first principles, the formation of Co/4d Frenkel point defects in the doped compounds is driven by electrons for trying to maintain the charge neutrality. The defects serve as extra scattering centers for charge carriers. As shown in Figure S15, the temperature-dependence index (β) of $\rho \sim T^\beta$ shows a gradual transition from 1.5 to 0.5 upon increasing the content of Sn, suggesting that the charge carriers experience a stronger alloy scattering which is following the existence of atomic point defects³⁴. Accordingly, the carrier mobility is also reduced because of the additional scattering, as shown in Figure S2a.

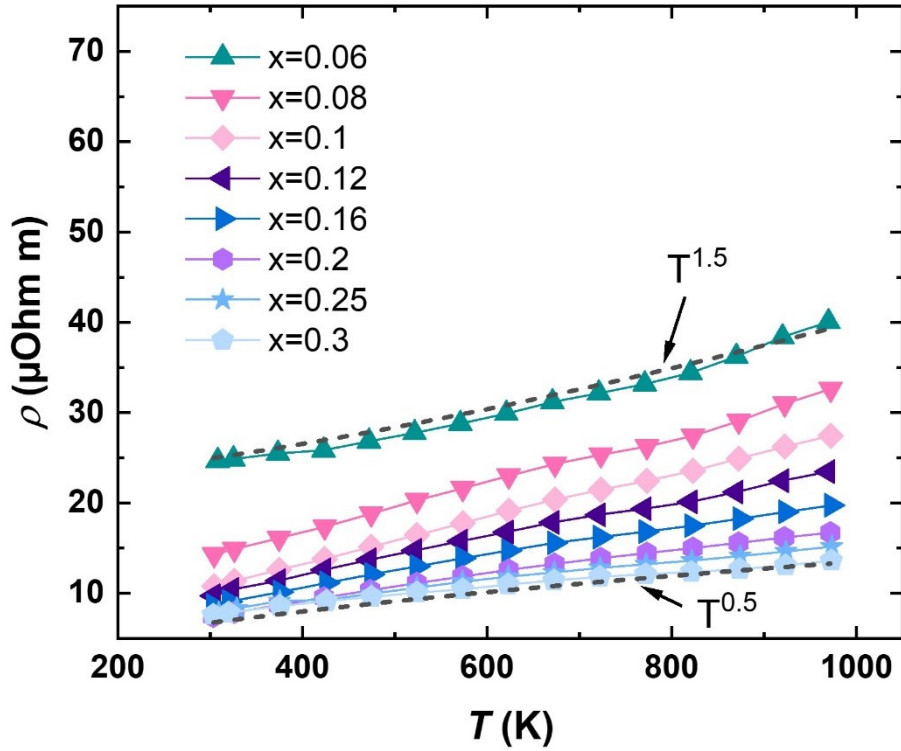


Figure S15. Temperature-dependent electrical resistivity of $\text{ZrCoSb}_{1-x}\text{Sn}_x$. The variation index (β) of $\rho \sim T^\beta$ shows a gradual transition of 1.5 to 0.5, suggesting a stronger alloy scattering upon increase the content of Sn.

Furthermore, the positively charged Co/4d defects yield n-type self-doping and modify the Fermi-level position. Accordingly, based on the reduced doping efficiency, we estimate the concentration of Co/4d Frenkel defects additionally. As shown in Figure S16a, we observe a doping efficiency of $\sim 70\%$ for the compound series $\text{ZrCoSb}_{1-x}\text{Sn}_x$. The reduced doping efficiency has two potential origins: 1) the insufficient ionization of the dopants due to the relative distance of the impurity level to the band edge; 2) charge compensation due to the formation of charge “killer” defects, such as Co/4d Frenkel defects in our case. By assuming the reduced $\sim 30\%$ doping efficiency entirely originating from the charge-compensation effect, we evaluate the concentration of Co/4d defect. Figure S16b shows the varied defect concentration with the dopant quantity with a +3 charge of Co/4d defects by summing the +2 charge of I_{Co} and the +1 charge of V_{Co} . Accordingly, the calculated defect concentrations are $\sim 2.2\%$ and $\sim 2.9\%$ under 20% and 30% Sn substitution at the Sb sites, respectively, which are consistent with other evaluating approaches in this work.

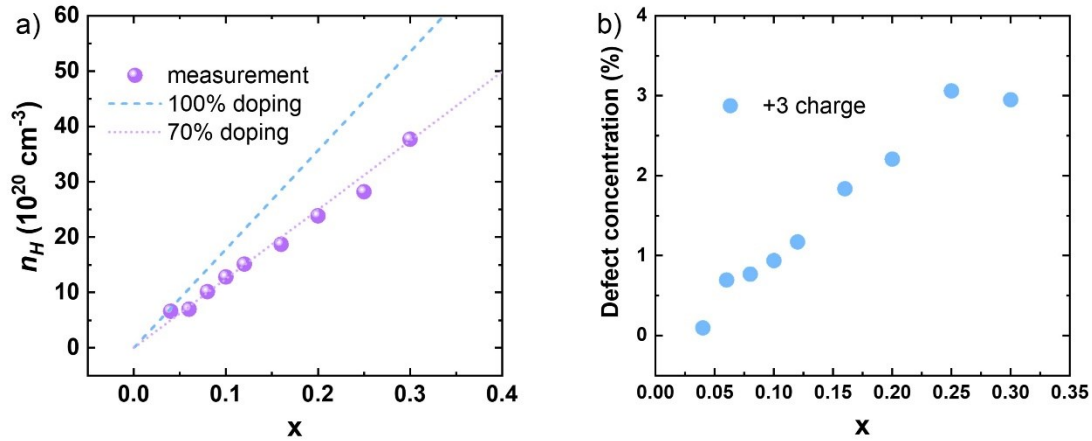


Figure S16. a) The carrier concentration of $\text{ZrCoSb}_{1-x}\text{Sn}_x$, showing a $\sim 70\%$ doping efficiency. b) The estimated Co/4d defect concentrations are $\sim 2.2\%$ and $\sim 2.9\%$ for $\text{ZrCoSb}_{0.8}\text{Sn}_{0.2}$ and $\text{ZrCoSb}_{0.7}\text{Sn}_{0.3}$, respectively, by considering a +3 charge of Co/4d Frenkel defect and that the reduced doping efficiency entirely originates from the charge-compensation effect.

References

1. G. Kresse and J. Furthmüller, *Physical Review B*, 1996, **54**, 11169-11186.
2. G. Kresse and J. Furthmüller, *Computational Materials Science*, 1996, **6**, 15-50.
3. P. E. Blöchl, *Physical Review B*, 1994, **50**, 17953-17979.
4. G. Kresse and D. Joubert, *Physical Review B*, 1999, **59**, 1758-1775.
5. J. P. Perdew, K. Burke and M. Ernzerhof, *Physical Review Letters*, 1996, **77**, 3865-3868.
6. S. Lany and A. Zunger, *Modelling and Simulation in Materials Science and Engineering*, 2009, **17**, 084002.
7. C. Freysoldt, J. Neugebauer and C. G. Van de Walle, *Physical Review Letters*, 2009, **102**, 016402.
8. A. Togo and I. Tanaka, *Scripta Materialia*, 2015, **108**, 1-5.
9. A. Togo, L. Chaput and I. Tanaka, *Physical Review B*, 2015, **91**, 094306.
10. R. He, H. Zhu, J. Sun, J. Mao, H. Reith, S. Chen, G. Schierning, K. Nielsch and Z. Ren, *Materials Today Physics*, 2017, **1**, 24-30.
11. R. He, L. Huang, Y. Wang, G. Samsonidze, B. Kozinsky, Q. Zhang and Z. Ren, *APL Materials*, 2016, **4**, 104804.
12. C. Fu, S. Bai, Y. Liu, Y. Tang, L. Chen, X. Zhao and T. Zhu, *Nature Communications*, 2015, **6**, 9144.
13. T. Wu, W. Jiang, X. Li, Y. Zhou and L. Chen, *Journal of Applied Physics*, 2007, **102**, 103705.
14. P. Debye, *Annalen der Physik*, 1912, **344**, 789-839.
15. C. Dames and G. Chen, *Journal of Applied Physics*, 2004, **95**, 682-693.
16. Z. Chen, X. Zhang, S. Lin, L. Chen and Y. Pei, *National Science Review*, 2018, **5**, 888-894.
17. A. Einstein, *Annalen der Physik*, 1911, **340**, 679-694.
18. P. G. Klemens, *Proc R Soc Lon Ser-A*, 1951, **208**, 108-133.

19. Z. Wang, J. E. Alaniz, W. Jang, J. E. Garay and C. Dames, *Nano Letters*, 2011, **11**, 2206-2213.
20. H.-S. Kim, S. D. Kang, Y. Tang, R. Hanus and G. Jeffrey Snyder, *Materials Horizons*, 2016, **3**, 234-240.
21. H. Zhao, B. Cao, S. Li, N. Liu, J. Shen, S. Li, J. Jian, L. Gu, Y. Pei, G. J. Snyder, Z. Ren and X. Chen, *Advanced Energy Materials*, 2017, **7**, 1700446.
22. H. Adachi, Y. Miyajima, M. Sato and N. Tsuji, *Materials Transactions*, 2015, **56**, 671-678.
23. G. K. Williamson and W. H. Hall, *Acta Metallurgica*, 1953, **1**, 22-31.
24. P. G. Klemens, *Proceedings of the Physical Society. Section A*, 1955, **68**, 1113-1128.
25. M. Roufosse and P. G. Klemens, *Physical Review B*, 1973, **7**, 5379-5386.
26. H. Zhu, R. He, J. Mao, Q. Zhu, C. Li, J. Sun, W. Ren, Y. Wang, Z. Liu, Z. Tang, A. Sotnikov, Z. Wang, D. Broido, D. J. Singh, G. Chen, K. Nielsch and Z. Ren, *Nature Communications*, 2018, **9**, 2497.
27. B. Liao, B. Qiu, J. Zhou, S. Huberman, K. Esfarjani and G. Chen, *Physical Review Letters*, 2015, **114**, 115901.
28. J. Bardeen and W. Shockley, *Physical Review*, 1950, **80**, 72-80.
29. Q. Ren, C. Fu, Q. Qiu, S. Dai, Z. Liu, T. Masuda, S. Asai, M. Hagihala, S. Lee, S. Torri, T. Kamiyama, L. He, X. Tong, C. Felser, D. J. Singh, T. Zhu, J. Yang and J. Ma, *Nature Communications*, 2020, **11**, 3142.
30. B. Abeles, *Physical Review*, 1963, **131**, 1906-1911.
31. G. A. Slack, *Physical Review*, 1962, **126**, 427-441.
32. C. A. Ratsifaritana and P. G. Klemens, *International Journal of Thermophysics*, 1987, **8**, 737-750.
33. R. Gurunathan, R. Hanus, M. Dylla, A. Katre and G. J. Snyder, *Physical Review Applied*, 2020, **13**, 034011.
34. H. Xie, H. Wang, C. Fu, Y. Liu, G. J. Snyder, X. Zhao and T. Zhu, *Scientific Reports*, 2014, **4**, 6888.